ADVANCED MATERIALS
www.advmat.de

Materials Views
www.MaterialsViews.com

Asymmetric MoS_2/Graphene/Metal Sandwiches: Preparation, Characterization, and Application

Peter S. Toth, Matěj Velický, Mark A. Bissett, Thomas J. A. Slater, Nicky Savjani, Aminu K. Rabiu, Alexander M. Rakowski, Jack R. Brent, Sarah J. Haigh, Paul O'Brien, and Robert A. W. Dryfe**

Atomically thin semiconductors, monolayers of transition-metal dichalcogenides (TMDCs), are of increasing interest as possible substitutes for Pt in the catalysis of hydrogen evolution reactions (HERs).[1] One of the most studied members of the TMDC family is molybdenum disulfide (MoS_2), used as a catalyst in HER because of its low cost, high chemical stability, and good electrocatalytic properties.[2] Unfortunately, bulk MoS_2 has poor conductivity, which is attributed to the lateral transfer of electrons along the layered structure of MoS_2 nanosheets.[2c] Graphene (GR), the first isolated single atomic layer,[3] composed of sp^2-hybridized carbon atoms, has good conductivity, high chemical durability, and a large surface area.[4] For this reason, it has become an important substrate for composite materials in catalysis research and energy storage devices.[5]

The different species of 2D layered materials can be stacked to form heterostructures, producing novel physical and chemical properties.[6] There have been significant prior studies demonstrating fabrication of MoS_2 and GR composites to enhance the catalysis of the most versatile energy storage system and energy carrier, i.e., hydrogen gas.[7] These 2D layered materials are excellent candidates for applications in electrochemical energy storage because of their high available surface area and versatile electronic structure.[8]

The question of the relative chemical activity of basal planes compared to the much more active edge planes (primarily in the case of GR) is still an open subject,[9] as quantifying differences in edge dimensions is challenging due to the inherently high surface energy.[1b,10]

Liquid/liquid self-assembly techniques consist of the dispersion of nanoparticles (NPs) in a hydrophilic or hydrophobic phase, followed by the driving of NPs to the oil/water interface using mechanical agitation or with the assistance of an inducing agent.[11] The interface between two immiscible electrolyte solutions (ITIES) is a special form of the generic liquid/liquid interface, where the presence of electrolyte in both phases provides external control over charge transfer, such as ion, electron, and proton-coupled electron transfers.[12] GR self-assembly at various organic/water interfaces has received much attention recently, as the assembled films offer the possibility of straightforward transfer, with the specific aim of preparing transparent or modified electrode materials.[13] Self-assembly of WSe_2 flakes has also been demonstrated at the interface of two immiscible nonsolvents (ethylene glycol and hexane).[14] However, to date, there is a lack of ordered assembly of layered TMDCs or their composites at the ITIES. In fact, only a small body of work has considered the construction of novel composites at the ITIES, i.e., metal-NP-decorated, low-dimensional carbon materials[15] and bimetal GR sandwiches.[16] Moreover, functionalization of the single-layer GR and preparation of the sandwiched structures, such as building up modified layers by adding them on top of one another to form doped GR papers or layered structures, altering topology as well as electronic structure, have also been reported recently.[17]

Here, we have fabricated a range of asymmetrically dual-functionalized GR-based nanoclusters, including layered MoS_2 and metal NPs on the top-side and metal NPs on the under-side. The resulting semiconductor/GR/metal sandwich structures have been characterized using a wide range of microscopic and spectroscopic techniques, including 3D electron tomography. We report three- and four-electrode configuration electrochemical measurements using the resultant nanocomposites to demonstrate the capability of the heterostructures for HER and enhanced capacitance performance.

The various MoS_2/GR heterostructures were obtained from either chemical vapor deposition (CVD)-grown, or liquid-phase exfoliated MoS_2 flakes and CVD-grown GR monolayers. The vertically aligned CVD-grown MoS_2 nanosheets (hereafter, $vMoS_2$) and the liquid-phase exfoliated MoS_2 flakes (hereafter, $eMoS_2$) were used to decorate the top-side of the GR, forming the $vMoS_2$/GR and $eMoS_2$/GR nanocomposites, respectively (**Figure 1**). The $eMoS_2$ flakes were assembled at the ITIES using ultrasonic agitation, while the $vMoS_2$ nanosheets were transferred from the Si/SiO_2 (the substrate for growth) to aqueous solution through etching of the Si/SiO_2 substrate by potassium hydroxide (KOH) solution. The $eMoS_2$ and $vMoS_2$ nanosheets were "fished out" from the organic/water or water/air interfaces, respectively, using CVD GR supported on a copper foil.

Dr. P. S. Toth, Dr. M. Velický, Dr. M. A. Bissett, Dr. N. Savjani, A. K. Rabiu, Prof. P. O'Brien, Prof. R. A. W. Dryfe
School of Chemistry
University of Manchester
Oxford Road, Manchester M13 9PL, UK
E-mail: peter.toth@manchester.ac.uk; robert.dryfe@manchester.ac.uk

Dr. T. J. A. Slater, A. M. Rakowski, J. R. Brent, Dr. S. J. Haigh, Prof. P. O'Brien
School of Materials
University of Manchester
Oxford Road, Manchester M13 9PL, UK

This is an open access article under the terms of the Creative Commons Attribution License, which permits use, distribution and reproduction in any medium, provided the original work is properly cited.

DOI: 10.1002/adma.201600484

© 2016 The Authors. Published by WILEY-VCH Verlag GmbH & Co. KGaA, Weinheim

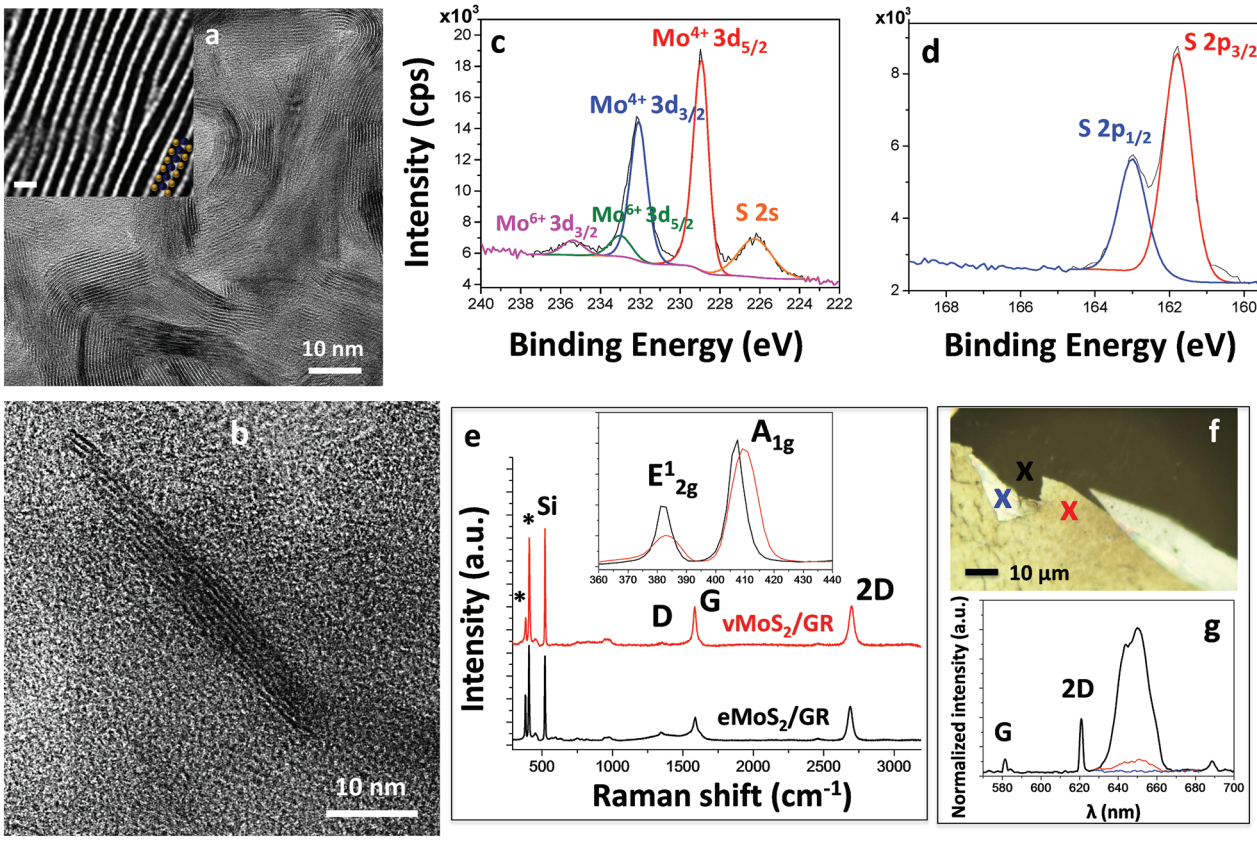

Figure 1. Characterization of the layered MoS_2/GR heterostructures: a) high-resolution transmission electron microscopy (HRTEM) image of vMoS_2/GR; the inset depicts the three atomic planes in the sequence of S–Mo–S (scale bar corresponds to 1 nm); b) the HRTEM image of the eMoS_2/GR. c,d) High-resolution XPS spectra of vMoS_2/GR show the Mo^{4+} 3d/S 2s/Mo^{6+} 3d (c) and S 2p (d) binding regions; the suborbitals are labelled. e) Raman spectra representing the two main MoS_2 bands (marked by asterisks and magnified by inset), the Si band, and the graphene peaks for eMoS_2/GR and vMoS_2/GR, respectively. f) Optical image of a free-standing vMoS_2/GR flake floating on a deionized water surface and g) the photoluminescence spectra of the GR (black), as well as thin (red) and thick (blue) portions of the vMoS_2 layer, recorded at the positions indicated via the colored crosses.

More details about the preparation and transfer of the MoS_2/GR structures are provided in the Experimental Section and in the Supporting Information (Section S1 and S2).

After transferring the vMoS_2 nanosheets to the single-layer GR, their well-aligned layered structure is maintained. Each of the layers consist of three covalently bonded atomic sheets, i.e., S–Mo–S (Figure 1a), with a layer-to-layer distance of about 6 Å, in agreement with literature values.[10] X-ray photoelectron spectroscopy (XPS) spectra of the vMoS_2 nanosheets are presented in Figure 1c,d, the position and shape of the Mo 3d and S 2p doublets confirm that the MoS_2 is present exclusively as the semiconducting 2H phase.[18] The apparent shoulder present on the Mo^{4+} $3d_{3/2}$ peak (Mo^{6+} $3d_{5/2}$, green peak at ≈233 eV in Figure 1c), and another component, Mo^{6+} $3d_{3/2}$ at ≈235 eV, are attributed to mild oxidation of the molybdenum ions (Mo^{4+} to Mo^{6+})[2a,b] (additional XPS surface analysis can be found in Section S7 in the Supporting Information). The electron microscope images of the eMoS_2/GR structures in Figure 1b indicate a less uniform coverage of the eMoS_2 on the monolayer GR compared to the vMoS_2/GR nanocomposite. The variable thickness of the eMoS_2 flakes can be seen, with flake thicknesses estimated to be mostly 3–10 layers, as illustrated by Figure 1b. The Raman spectra of the eMoS_2/GR (black curve) and vMoS_2/GR (red curve) heterostructures are shown in Figure 1e. The expected peaks' characteristic of single-layer GR are observed: the D peak that corresponds to edges and defects, the G peak that is associated with the E_{2g} vibration mode of the sp^2 bonds, and the 2D peak that is caused by the scattering of two phonons which can occur independently of defects. The inset in Figure 1e highlights the presence of peaks corresponding to the most intense phonon modes of MoS_2, including the in-plane (E^1_{2g}) and out-of-plane (A_{1g}) lattice vibrations,[19,20] which exhibit hardening and softening, respectively. The Raman spectra from the GR on the under-side of both kinds of MoS_2 material showed upshifts of both the G and 2D bands. In the case of the G peak, the increase is observed from 1585.5 cm^{-1} (pristine CVD GR) to 1587.2 cm^{-1} (eMoS_2/GR), and 1587.5 cm^{-1} (vMoS_2/GR), while the 2D band is upshifted from 2677.1 cm^{-1} (pristine CVD GR) to 2687.8 cm^{-1} (eMoS_2/GR), and 2697.3 cm^{-1} (vMoS_2/GR). The width of the 2D band increases from 30.4 cm^{-1} (pristine CVD GR) to 40.7 cm^{-1}, and 43.5 cm^{-1} for eMoS_2/GR, and vMoS_2/GR heterostructures, respectively. The frequency upshifts of the G and 2D bands combined with the increase in 2D width indicate p-type doping,[21] which can be explained by interlayer coupling between GR and MoS_2,[22] and photoinduced electron transfer

© 2016 The Authors. Published by WILEY-VCH Verlag GmbH & Co. KGaA, Weinheim

from MoS_2 to GR,[23] due to excitation by the visible light (532 nm) irradiation of the Raman laser. When comparing the Raman spectra of $eMoS_2$/GR (black) and $vMoS_2$/GR (red), the difference in the intensity ratio ($I_{E^1_{2g}}/I_{A_{1g}}$) is clearly evident, the ratio for the $eMoS_2$/GR sample is ≈0.49 while the ratio for the $vMoS_2$/GR sample is ≈0.24, verifying that the $vMoS_2$/GR sample is indeed edge-terminated and vertically aligned[10,24] (detailed comparison of the $vMoS_2$ and basal planes is given in Section S3 in the Supporting Information).

Considering the band structure difference between the indirect-bandgap semiconductor of bulk MoS_2 to the direct-bandgap semiconductor in monolayer MoS_2, we would not expect to see any photoluminescence (PL) in the case of the $vMoS_2$/GR heterostructure, which was true for the samples supported on the Si/SiO_2 wafer before transfer to the GR. Surprisingly, PL appeared when measuring free-standing $vMoS_2$/GR floating on the surface of deionized water. The optical micrograph (Figure 1f) displays this floating $vMoS_2$/GR, with "singly" coated (≈50 nm), folded nanosheets (≈150 nm), and the exposed part (top of image) showing the GR support (characterization of these height profiles is given in Section S3 in the Supporting Information). The PL was strongest for the exposed GR surface (black curve in Figure 1g), indicating breakage of some thin (mono- or bilayer) $vMoS_2$ nanosheets during its transfer and subsequent heterostructure formation. The negligible quenching of the observed strong PL response indicates that the interlayer charge transfer, which results from the interaction between the MoS_2 and GR sheets, is relatively weak and is similar to what has been observed for mechanically stacked heterostructures.[23] This is in contrast with similar CVD-grown heterostructures where strong quenching of the PL from the MoS_2 grown on GR was observed.[23]

The pristine and MoS_2-decorated single-layer GR can be functionalized using metal NPs on either both sides, or solely on the under-side. A number of MoS_2/GR/metal sandwiches have been prepared using a polarizable organic/water interface.

Three kinds of functionalization of the GR layers were carried out. First, top-side decoration was performed using semiconductors ($eMoS_2$, $vMoS_2$) or metal NPs (Pd, Pt, Au, Ag). Second, under-side decoration of metal NPs achieved at the organic/water interface using either the spontaneous deposition route (Pd, Au, Ag), or electrochemical deposition (Pd, Pt), or by the controlled etching of the Cu foil used for the CVD growth of GR (Cu). In the latter special case, the exact amount of Cu NPs remaining on the GR could be precisely determined by control of the etching conditions (Supporting Information, Section S7). Third, bi-facial decoration (asymmetric or symmetric) was achieved by decorating the GR on the top-side, before the decorated GR-based hybrid is subsequently functionalized on the under-side. Hereafter, the resultant nanocomposites are termed to signify the relative positions of the species to the GR layer, e.g., if the top- and under-sides of the GR are decorated with $vMoS_2$ nanosheets and Pd NPs, respectively, the name of the nanocluster will be $vMoS_2$/GR/Pd. Examples of several dual-decorated CVD GR-based nanostructures, such as $vMoS_2$/GR/Pd (top-part of figure), $eMoS_2$/GR/Pd (from the left to right in the bottom of figure), Pt/GR/Cu, and Pd/GR/Pd, are shown in **Figure 2**.

The functionalization of CVD GR with metal NPs at an interface has been described previously,[16,25] but a description is also

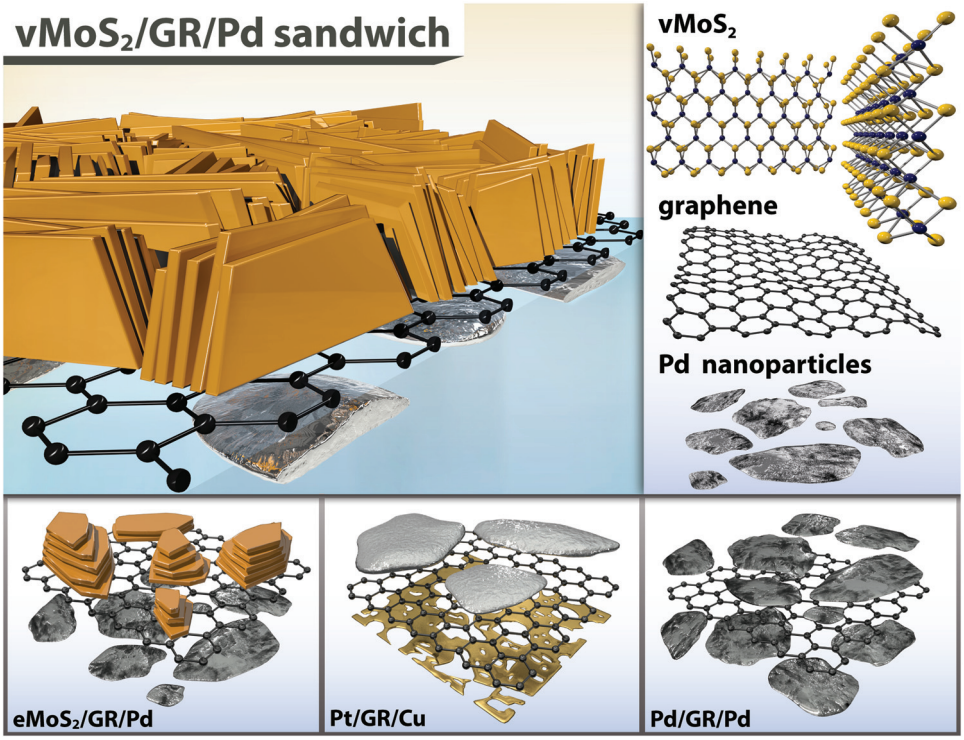

Figure 2. 3D illustration of the $vMoS_2$/GR/Pd sandwich (top). Schematics of the $eMoS_2$/GR/Pd, Pt/GR/Cu, and Pd/GR/Pd sandwiches (bottom of image, from left to right).

© 2016 The Authors. Published by WILEY-VCH Verlag GmbH & Co. KGaA, Weinheim

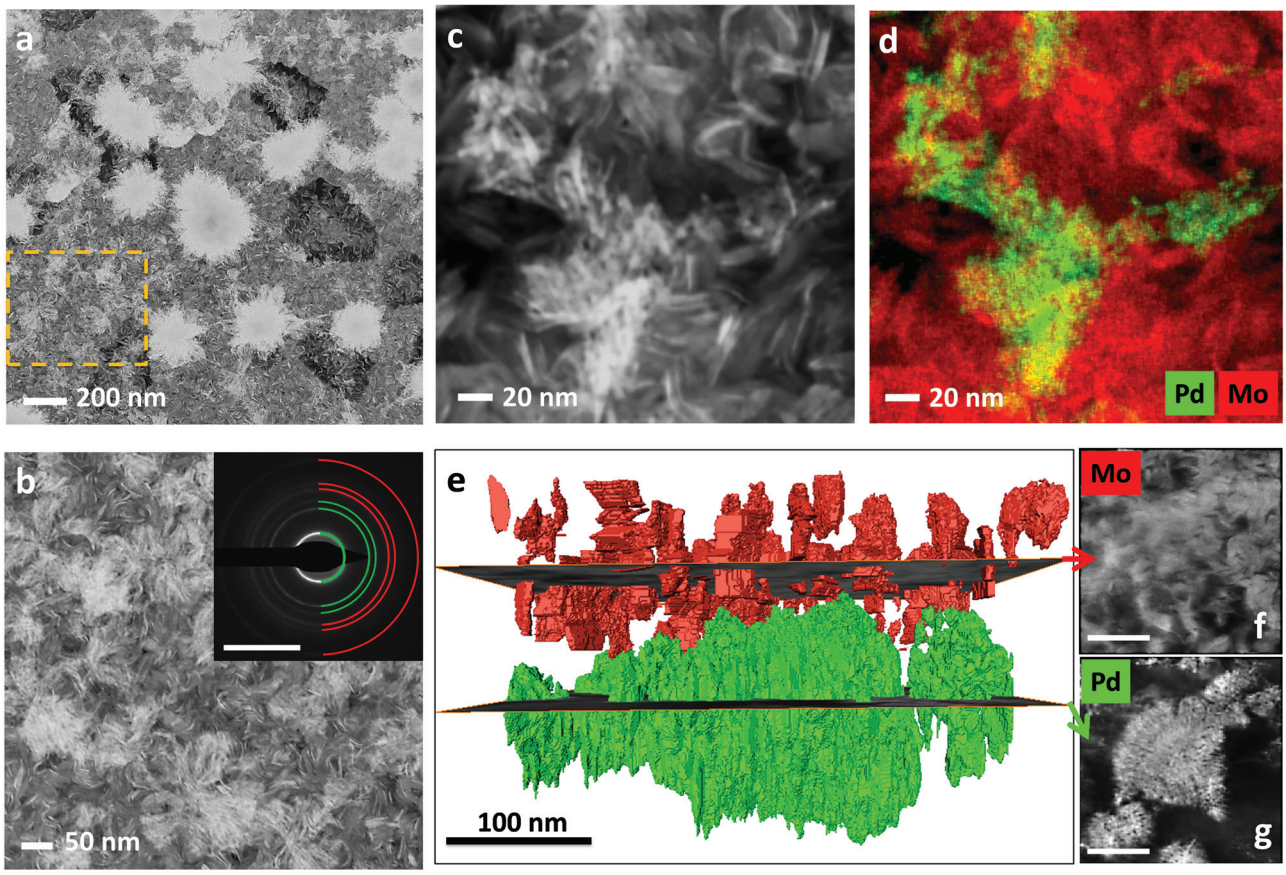

Figure 3. a–d) HAADF-STEM images and a STEM-EDX elemental map of the graphene-based $vMoS_2$- (top-side) and Pd- (under-side) decorated nanoclusters ((d) acquired in the same region as (c)). The region indicated by the yellow dashed line in (a) is shown in (b). The electron DP image (scale bar corresponds to 5 nm^{-1}) of $vMoS_2$/GR/Pd is depicted in the inset of (b) with the rings corresponding to the expected lattice spacings of MoS_2 (green) and crystalline Pd (red), representing the (002), (100), and (101) and the (111), (002), and (202) reflections for MoS_2 and Pd, respectively. e) 3D surface visualization of the segmented $vMoS_2$/GR/Pd sandwich analyzed by HAADF-STEM electron tomography, displaying the surface visualization of the segmented Pd (green) and $vMoS_2$ (red) volumes. f,g) Slices through the reconstruction at the positions indicated, showing the $vMoS_2$ "layer" on the top-side (f) and Pd "layer" on the under-side (g); the scale bars correspond to 100 nm. The interfacial deposition time was 1 min of Pd NPs decoration to under-side of GR.

given here in the Experimental Section. Briefly, the MoS_2/GR heterostructures are assembled at the polarizable organic/water interface, then the hybrid material is transferred to the surface of an aqueous layer/phase before a lower density organic phase is layered on top. The resulting ITIES offers the possibility to induce metal-NP deposition on the assembled GR using metal precursors in the aqueous phase and an organic phase electron donor, employing either simple galvanic displacement reactions (as a function of potential difference) or direct potential control.[25] The MoS_2/GR at the interface was functionalized with Pd NPs by adding tetrachloropalladate ($PdCl_4^{2-}$) in the aqueous phase and decamethylferrocene (DecMFc) as the electron donor agent in the organic phase respectively (the cell composition is shown in Composition 1).

High-angle annular dark-field (HAADF) scanning transmission electron microscopy (STEM) images (**Figure 3**a–c) show the $vMoS_2$/GR/Pd sandwich, visualizing the vertically aligned MoS_2 structure and the bright Pd NPs (Figure 3b). The size distribution of individual Pd NPs is ≈5–10 nm (Figure 3c) and these individual NPs assemble into "snowflake-like" structures (≈100–200 nm)[25] (Figure 3a), respectively. Confirmation that the "snowflake-like" structures correspond to Pd (green) and the stacked flakes correspond to Mo (red) is provided by STEM energy-dispersive X-ray (EDX) spectrum imaging (Figure 3d). Further confirmation of the presence of both Pd and MoS_2 is provided through electron diffraction patterns (DPs) (inset of Figure 3b), displaying polycrystalline rings characteristic of Pd and MoS_2. Moreover, a HAADF-STEM tomography reconstruction[16,26] of a small area (Figure 3e) shows the vertical displacement of the MoS_2 and Pd layers, where the different materials can be segmented due to their distinct morphologies. This reconstructed area is densely decorated by Pd NPs, showing clearly the "sandwich structure" of the $vMoS_2$ nanosheets on the top-side (Figure 3f) and the Pd NPs on under-side of the GR sheet (Figure 3g).

The same reaction was undertaken on the under-side of the $eMoS_2$/GR structure using $PdCl_4^{2-}$, $AuCl_4^-$, and Ag^+ in the aqueous phase, resulting in $eMoS_2$/GR/Pd, $eMoS_2$/GR/Au, and $eMoS_2$/GR/Ag sandwiches, respectively (further characterization is given in Section S5 in the Supporting Information). The other route to decorate the interface-assembled heterostructures is via potentiodynamic metal-NP deposition (using cyclic

© 2016 The Authors. Published by WILEY-VCH Verlag GmbH & Co. KGaA, Weinheim

voltammetry).[27] This cell contained either $PdCl_4^{2-}$ or $PtCl_4^{2-}$ in the aqueous phase and 1,1′-dimethylferrocene (DMFc) in the organic phase (Composition 2).

In this case, DMFc acts as the electron donor, and during its electro-oxidation through the assembled MoS_2/GR heterostructures at the ITIES, the reduction of the $PdCl_4^{2-}$ to Pd NPs occurs at the aqueous side of the interface on the under-side of the MoS_2/GR, by analogy with the similar Pd electrodeposition on the pristine CVD GR assembled at the ITIES.[28] The potential cycling for the electrodeposition is given in Section S6 in the Supporting Information. More evidence for the asymmetrically dual-decorated GR sandwiches can be found in the videos of the aligned HAADF-STEM tilt series' and final reconstructions provided as Supporting Information (Movie S1 and S2).

Electrochemical measurements using microdroplets[9a,c,29] were performed in order to investigate the HER catalytic performance and to determine the interfacial capacitance for the different GR-based composites. In order to assess the catalytic activity toward HER, polarization curves of five samples (GR, $vMoS_2$, $vMoS_2$/GR, $eMoS_2$/GR/Pd, and $vMoS_2$/GR/Pd) were measured in aqueous droplets containing 0.1 M HCl and 6 M LiCl (**Figure 4**a).

The Tafel slopes estimated from the linear portions of the polarization curves (Figure 4a) using the Tafel equation (Equation S2, Section S10, Supporting Information) for all the studied samples (Figure 4b). The edges sites are believed to be the most catalytically active and thus one would expect the $vMoS_2$ to naturally have superior performance.[1b] Indeed as predicted, $vMoS_2$ exhibits 112.0 ± 0.99 mV dec^{-1} at a low overpotential, the current density is high, with the smaller Tafel slope corresponding to a faster increase of HER rate.[30] While, the $vMoS_2$/GR/Pd nanocomposite exhibits superior activity with the smallest Tafel slope value of 71.0 ± 0.93 mV dec^{-1} at the lowest overpotential. However, lower Tafel slopes were reported previously,[2a,30] e.g., those of the electrochemical tuned vertically aligned MoS_2 nanofilms (44 mV dec^{-1})[2a] or MoS_2/reduced GR oxide hybrid modified glassy carbon electrode (41 mV dec^{1}).[7a] In acidic media there are three operative reaction mechanisms[31] for the HER: first the initial discharge step (Volmer reaction where the Tafel slope, b is around 120 mV dec^{-1}), which can be followed by either an electrochemical desorption step (Heyrovsky reaction, $b \approx 40$ mV dec^{-1}) or a recombination step (Tafel reaction, $b \approx 30$ mV dec^{-1}). Considering the 71.0 mV dec^{-1} Tafel slope found for the $vMoS_2$/GR/Pd nanocomposite, it is likely the combination of initial discharge and electrochemical desorption steps could be the rate-limiting processes. A recent report has discussed the use of the chemically exfoliated MoS_2 nanosheets, and the relative efficiency of hydrogen evolution from the 1T and 2H phases of the MoS_2 nanosheets.[32] The reported superior electrocatalytic activity is obtained only in the case of the high concentration of 1T MoS_2 particles, while the semiconducting 2H phase's activity for HER reaction can be improved by increasing its conductivity through doping with SWNTs, we note that Tafel slopes similar to those reported here were found for the 2H case.

The capacitive performance of the GR hybrid films was electrochemically tested to determine the electric double-layer capacitances (C) for each sample (calculated using Equation S3, Section S10, Supporting Information). The specific capacitance (C_{sp}) values were calculated using the C and surface area

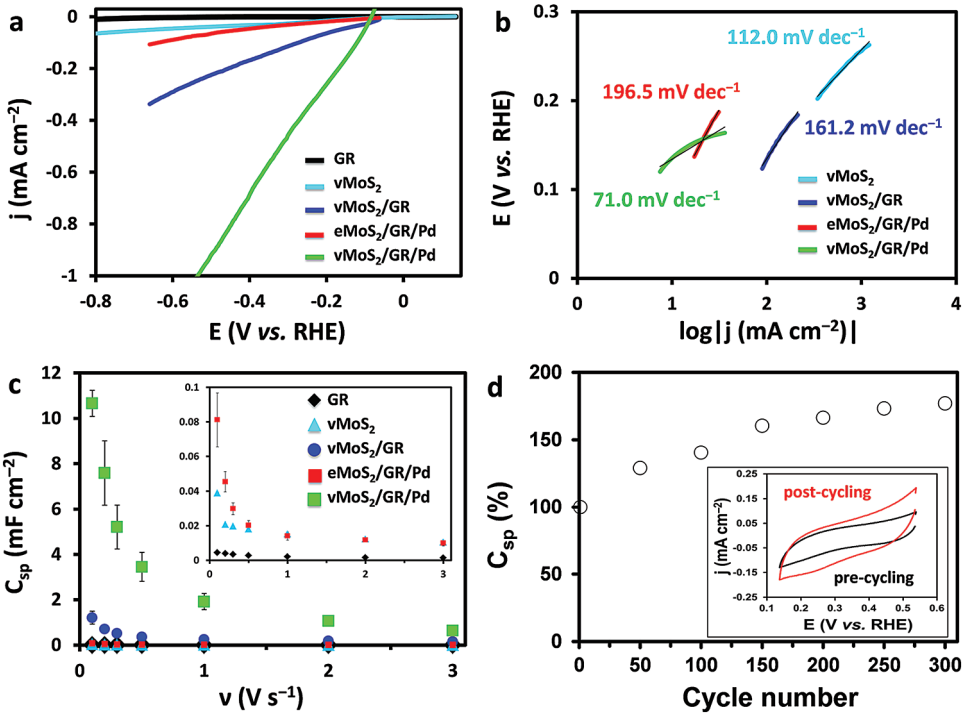

Figure 4. a) The HER polarization curves obtained on the composite materials, at 5 mV s^{-1} scan rate. b) Tafel slopes of HER reactions. c) Specific capacitance versus scan rate, the inset is the magnified GR, $vMoS_2$, $eMoS_2$/GR/Pd signals, respectively. d) Plot of the increase in specific capacitance (%) with continued cycling; the pre- and postcycling voltammograms before and after 300 cycles are shown in the inset.

© 2016 The Authors. Published by WILEY-VCH Verlag GmbH & Co. KGaA, Weinheim

values. The dependence of the C_{sp} on scan rate is depicted in Figure 4c, showing the well-known inverse correlation with increasing scan rate due to the transport limit on the supply of ions.[8b,c] At 100 mV s^{-1} the calculated specific capacitance for the $vMoS_2$/GR/Pd (10.7 mF cm^{-2}) is ≈9, 130, 270, and 2400 times larger than that for $vMoS_2$/GR (1.21 mF cm^{-2}), $eMoS_2$/GR/Pd (81.2 μF cm^{-2}), $vMoS_2$ (38.9 μF cm^{-2}), and GR (4.4 μF cm^{-2}), respectively (Figure 4c). An ideal electric double-layer capacitor supercapacitors should possess extremely high stability with minimal degradation in performance with repeated charge/discharge cycles, while pseudocapacitors typically sacrifice cycling stability for increased energy density.[8c] Figure 4d shows the cycling stability of the $vMoS_2$/GR/Pd nanocluster over 300 cycles. There is a large increase (≈170%) when comparing the C_{sp} values precycling relative to postcycling. A prolonged cycling in order to check both electrical and mechanical stabilities up to 2000 cycles has shown durability of the $vMoS_2$/GR/Pd nanocomposite and further increase in capacitance (≈340%) observed. The heterostructures appear to be quite robust during the timescale used for measurements, although further long terms studies are required to ascertain their stability before practical applications are considered. This increased capacitance with continuous cycling has been reported previously for GR and MoS_2 composites, and was also attributed to the partial exfoliation with continued ion intercalation/deintercalation increasing the active surface area, termed "electroactivation."[8b,33] In the particular case of a dual-decorated GR sandwich ($vMoS_2$/GR/Pd), during the "electroactivation," the Li^+ ions can also penetrate through and incorporate into the porous metal nanostructures.

Both carbon nanotubes and GR assemblies at the ITIES, as well as exfoliated TMDCs in the aqueous phase, have received significant interest for applications in energy storage and conversion, mainly HER and the oxygen reduction reaction.[34] Considering the high HER activity measured and the enhancement in the case of the $vMoS_2$/GR/Pd, significant proton transfer through the GR single-layer must occur, either through defects or via the intrinsic proton conductivity,[35] in order to explain the enhanced catalytic and capacitive behaviors of the under-side functionalized composites (with Pd NPs on the under surface) versus the top-side only decorated composites. We have studied the catalytic role of the as-prepared dual-decorated GR-based composites in HER at polarized 6 M LiCl (aq)/DCB interfaces (Composition 3), between an aqueous acidic solution and a solution of DecMFc acting as a molecular electron donor in the organic phase (**Figure 5**). The reaction between DecMFc and aqueous H^+ catalyzed by adsorbed GR-based hybrid particles is depicted in the schematic (Figure 5a).

In the case of HER at the ITIES, the catalytic process occurs at high Galvani potential differences (which is defined as the potential difference between the aqueous and organic phase by convention[34a]), and not at negative reducing potentials as on a conventional solid electrode. The observed redox peaks between −0.1 V and −0.3 V correspond to the $DecMFc^+$ cation transfer, while the more positive redox activity (further than 0.0 V) corresponds to the HER (more details are given in Section S9

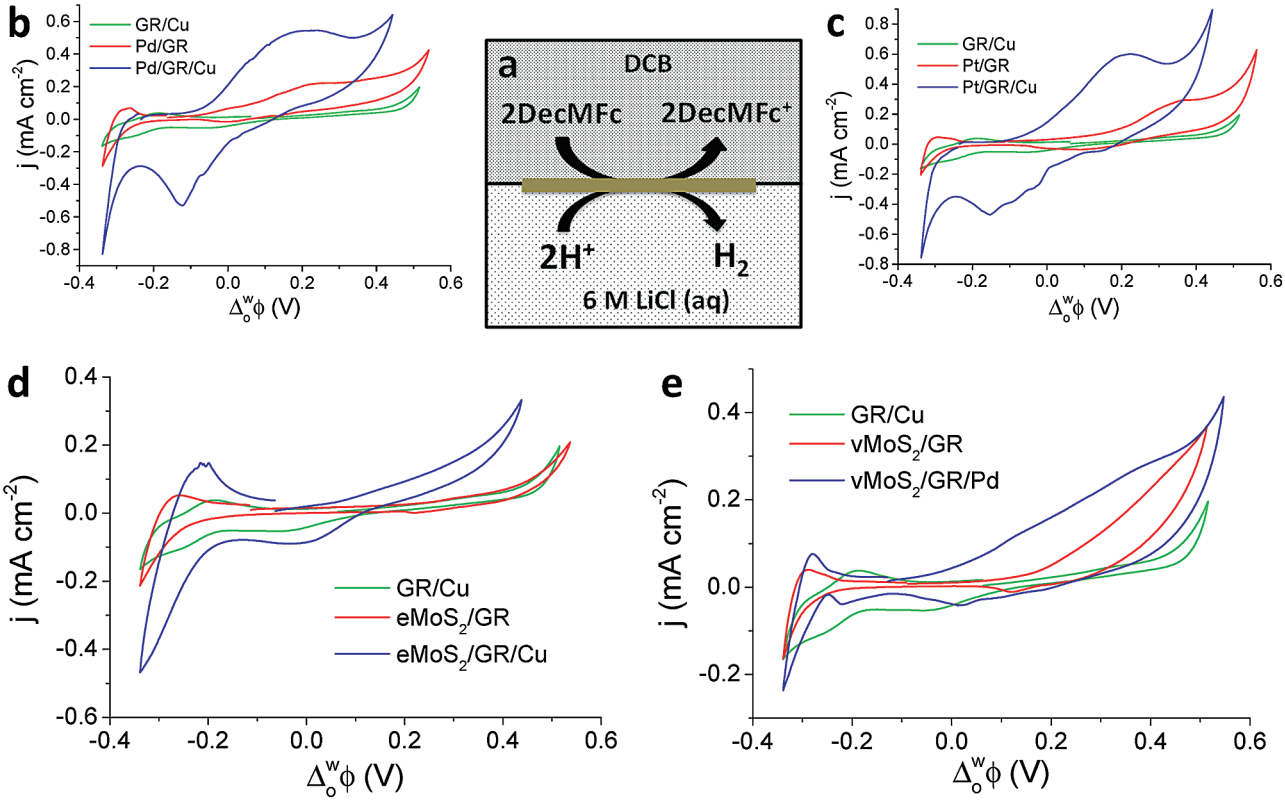

Figure 5. a) Schematic of the HER at the interface. b–e) Cyclic voltammograms at 6 M $LiCl_{(aq)}$/DCB interface, comparing Pd/GR (b), Pt/GR (c), $eMoS_2$/GR (d), and $vMoS_2$/GR (e) heterostructures assembled at the interface, using a scan rate of 50 mV s^{-1}.

© 2016 The Authors. Published by WILEY-VCH Verlag GmbH & Co. KGaA, Weinheim

in the Supporting Information). In order to investigate the as-prepared dual-decorated composites to enhance the HER at the 6 M $LiCl_{(aq)}$/DCB interface, the Pt/GR, Pd/GR, $eMoS_2$/GR, and the $vMoS_2$/GR-based heterostructures (under-side was functionalized with residual Cu particles) were compared in Figure 5b–e, respectively. Furthermore, the assembly of individual, macroscopic (cm^2 scale) GR-based catalyst material at the ITIES containing redox active species for HER minimizes the possibility of "uncontrolled adsorption" or sedimentation of the exfoliated TMDCs particles at the interface.[34d] For all cases, the top-side decorated sample, e.g., $vMoS_2$/GR (red curves) was compared to the dual-functionalized, e.g., $vMoS_2$/GR/Pd (blue curves) and the GR/Cu composites (green curves), employing the GR/Cu as a standard to compare with the top-side decorated layered semiconductors ($eMoS_2$ or $vMoS_2$) composites and the both sides decorated ones, respectively. In the case of the under-side functionalized nanocomposites (e.g., GR/Cu), the protons are adsorbed on the catalyst surface on the under-side of GR, which conducts the electrons from the DecMFc oxidation to the protons, leading to fast electron transfer ($\Delta_o^w\phi$ = +0.183 V). Employing the top-side decorated hybrids, the protons have to transfer to the catalyst surface on the top-side through the GR single-layer[35] and reduction must occur there (e.g., $\Delta_o^w\phi$ = –0.109 V for Pt/GR). However, in the case of the asymmetrically dual-functionalized composites, the protons can be either adsorbed on the under-side of the catalyst and reduced there, or transfer to the top-side of the catalyst through the monolayer GR, or do both leading to an enhanced activity: $\Delta_o^w\phi$ = –0.022 V and $\Delta_o^w\phi$ = –0.091 V for $eMoS_2$/GR/Cu and $vMoS_2$/GR/Pd (close to the Pt/GR/Cu composite, where $\Delta_o^w\phi$ = –0.123 V), respectively. Previous literature has reported a range of catalysts employed to increase the rate of HER reaction at the ITIES, including Pt, Pd,[36] and Cu[37] NPs. Proton reduction can occur either in the aqueous or in DCB phase, the proton reduction potential in the DCE phase has been reported as 0.55 V.[38] Herein, the enhanced activity is indicated with the lower overpotential values for HER at the interface. It is the combination of the highly catalytically active palladium combined with the MoS_2 which leads to the excellent electrocatalytic performance of the composite for HER. Considering the deeper understanding of the effect of GR–based nanocomposites for the different catalysis, further investigations and the isolation of the operative factors will be the subject of additional studies, such as the investigation of the different metal NPs with different behaviors and comparison of several conditions (pH, different thickness of the heterostructures, and varying their compositions).

In summary, we have synthesized and characterized various MoS_2/GR heterostructures, including CVD-grown and liquid-phase exfoliated MoS_2 nanosheets and flakes, respectively. In our work, the interlayer coupling between the MoS_2 and GR would be expected to be most similar to the mechanically stacked structures which also show very little quenching.[23] These hybrid heterostructures were functionalized with metal NPs (Au, Ag, Pd, Pt, Cu) on the opposite side to the MoS_2, forming asymmetric dual-side decorated GR sandwiches, via both spontaneous and potential-controlled procedures.

The different nanocomposites show diverse catalytic activities, with the best Tafel slope for the HER found to be 71.0 mV dec^{-1} for the $vMoS_2$/GR/Pd sandwich, outperforming the other MoS_2 containing composites (161.2–196.5 mV dec^{-1}). This $vMoS_2$/GR/Pd sandwich has exhibited enhanced catalytic activity compared to both the pristine materials and the other heterostructures studied in this work. Considering the ≈200% and ≈340% increase during the cycling stability measurements in the case of 300 and 2000 cycles, respectively, this hybrid structure is also a promising candidate as a supercapacitor electrode. Additionally, the dual-decorated GR sandwiches, mainly the $vMoS_2$/GR/Pd hybrid, demonstrated enhanced HER activity at a 6 M $LiCl_{(aq)}$/DCB interface.

The key finding is the creation of a unique platform of asymmetrically functionalized MoS_2/GR heterostructures, and the investigation of fundamental electrocatalytic properties of these structures. Furthermore, this work leads to new prospects for assembly of liquid-phase exfoliated layered 2D semiconductors at polarizable organic/water interfaces, offering the platform for developing fundamental studies and exploiting them in energy storage and conversion, e.g., lithium intercalation and photoelectrochemical hydrogen production. Moreover, this opens up further, new vistas for GR asymmetric functionalization including composite structures incorporating 2D semiconductors, metal NPs, or materials with switchable redox systems, i.e., conducting polymers. Through inclusion of two different catalyst materials on each side of the GR single-layer, the asymmetrically dual-decorated GR-based composites provide an ideal platform to catalyze several biphasic reactions, for example an enhancement of two different redox reactions simultaneously occurring in the organic and aqueous phases respectively.

Experimental Section

Preparation of $eMoS_2$/GR and $vMoS_2$/GR Heterostructures: The MoS_2 dispersions ($eMoS_2$) were created by liquid phase exfoliation and the large-area, thickness-controlled, vertically aligned MoS_2 nanosheets ($vMoS_2$) were prepared by sulfurization of thin metal films (CVD method), as reported previously.[39] The detailed preparation procedures for both kinds of MoS_2 material, together with the UV–vis characterization and concentration calibration for $eMoS_2$ solutions are provided in the Supporting Information (Section S2 and S3).

The $eMoS_2$ flakes' assembly at the organic/water interface was established according to the procedure for few-layer GR flakes' assembly, as described elsewhere.[15b] Briefly, an aliquot of the $eMoS_2$ dispersion (20 μg mL^{-1}) with the organic electrolyte solution in DCB was placed in contact with an equal volume of aqueous phase, and then self-assembly of the $eMoS_2$ flakes at the interface was achieved using ultrasonic agitation (15 min). Both phases contained supporting electrolytes, 0.1 M $LiClO_4$ in the aqueous phase and 0.1 M $TBAClO_4$ in the organic phase, respectively. After 2 h, the $eMoS_2$ flakes assembled at the interface in a thin film. Subsequently, a part of this film was "fished out" using the CVD GR lying on the Cu foil and the sample was dried, forming the $eMoS_2$/GR structures (Figure S2, Supporting Information).

The $vMoS_2$ thin sheets were transferred to CVD GR to form the $vMoS_2$/GR heterostructure (Figure S7, Supporting Information). The transfer was carried out by spin-coating the $vMoS_2$ sheet with 3% 950 K poly(methyl methacrylate) (PMMA) solution (in anisole) on the Si/SiO_2 substrate at 3000 rpm for 60 s using SPIN200i-NPP spin processor (SPS-Europe B.V.). This resulted in the formation of a PMMA/$vMoS_2$/Si/SiO_2 substrate multilayer structure (Figure S7b, Supporting Information). The Si/SiO_2 was etched from underneath the PMMA/MoS_2 multilayer by 2 M KOH (Figure S7c, Supporting Information), then the SiO_2 between the MoS_2 and the Si substrates was completely etched, leaving

© 2016 The Authors. Published by WILEY-VCH Verlag GmbH & Co. KGaA, Weinheim

PMMA/vMoS_2 multilayers floating on the KOH surface (Figure S7d, Supporting Information), and then cleaned three times by transfer to pure water, resulting in a pure PMMA/vMoS_2 (Figure S7e, Supporting Information). The remaining PMMA/vMoS_2 heterostructure was then "fished out" with a CVD GR monolayer lying on copper foil, forming the PMMA/vMoS_2/GR/Cu foil stack (Figure S7f, Supporting Information), then after drying the sample the Cu foil was etched from underneath the PMMA/vMoS_2/GR multilayer by 0.5 M ammonium persulfate solution (Figure S7g, Supporting Information) and the remaining nanocomposite was "fished out" with an Si/SiO_2 wafer, and then cleaned three times by transfer to pure water, resulting in a PMMA/vMoS_2/GR stack. The pure PMMA/vMoS_2/GR was transferred to aqueous phase (Figure S7h, Supporting Information) using an Si/SiO_2 wafer.

Preparation of Mono- or Bimetal Graphene Sandwiches: The top-side decoration of the GR with Pd or Pt NPs was performed using a simple galvanic displacement for the nucleation of Pd or Pt NPs.[16] The underlying copper foil acted as an electron donor under the GR monolayer and transferred electrons to the noble metal. Alternatively, spontaneous Pd NP deposition on the under-side of the GR was achieved at the interface-assembled CVD GR. An interfacial redox reaction between decamethylferrocene (DecMFc), which is the organic phase electron donor, and $PdCl_4^{2-}$ contained in the aqueous phase created GR/Pd layers.[28]

Characterization Techniques: Characterization of samples was performed following either the preparation or functionalization of the MoS_2/GR sandwich. These composite layers were fished out using either an Si/SiO_2 substrate or specifically prepared free-standing samples supported on holey carbon-coated nickel quantifoil grids (TAAB Laboratories Equipment Ltd.), dried in air for 15 min, then washed in an ethanol and isopropyl alcohol mixture (5 min) and then acetone (5 min), and finally blow-dried with nitrogen. To characterize the various GR-based sandwiches, Raman spectroscopy (Renishaw inVia, 532 nm laser excitation), scanning electron microscopy (SEM) (Philips XL30 ESEM-FEG), atomic force microscopy (Bruker MultiMode 8) measurements, and elemental analysis using XPS (Thermo Fisher Scientific, Inc.) and energy-dispersive X-ray spectroscopy (EDX in the SEM) were carried out. All of the measurements were obtained using the techniques at 3–5 different surface sites. Furthermore, HAADF-STEM imaging was performed on an FEI Talos F200X S/TEM with a high brightness X-FEG electron source and Super-X energy-dispersive silicon drift detectors. High-resolution EDX spectrum images were acquired in the Bruker Esprit software using the Talos' Super-X detector system. A tilt series for HAADF-STEM tomography was acquired using Xplore3D acquisition software at angular increments of 1° from −60° to +60°. Selected area electron diffraction patterns were acquired using a selected area aperture of ≈200 nm diameter and a camera length of 840 mm. The displayed errors are either standard deviations (arithmetic averages of multiple measured values) or absolute errors determined from the best-fit errors.

Applied Electrochemical Methods: The electrochemical experiments were performed using either a four- or three-electrode configuration (Supporting Information, Section S4). In both cases the electrochemical signal was measured using a PGSTAT302N potentiostat (Metrohm Autolab). All the potentials reported in this work were plotted on the reversible hydrogen electrode scale,[30] calculated from Equation S1 (see Section S10, Supporting Information). Cyclic voltammetry was employed for the interfacial electrodeposition of Pd or Pt NPs on MoS_2/GR, redox reactions at the interface, and capacitance measurements. Additionally, the HER was investigated by linear sweep voltammetry.

The Cell Compositions for the Experiments at the ITIES: 0.1 M $LiClO_4$ and 1×10^{-3} M $PdCl_4^{2-}{}_{(aq)}$ || 0.1 M $TBAClO_4$ and 2×10^{-3} M $DecMFc_{(o)}$ (Comp. 1)

$Ag/AgCl_{(s)}$ | 0.1 M LiCl and 1×10^{-3} M $PdCl_4^{2-}{}_{(aq)}$ || 10×10^{-3} M PTPPATPFB and 5×10^{-3} M $DMFc_{(o)}$ | 0.1 M LiCl and 1×10^{-3} M $BTPPACl_{(aq)}$ | $Ag/AgCl_{(s)}$ (Comp. 2)

$Ag/AgCl_{(s)}$ | 6 M LiCl and 100×10^{-3} M $HCl_{(aq)}$ || 10×10^{-3} M PTPPATPFB and 5×10^{-3} M $DecMFc_{(o)}$ | 0.1 M LiCl and 1×10^{-3} M $BTPPACl_{(aq)}$ | $Ag/AgCl_{(s)}$ (Comp. 3)

Supporting Information

Supporting Information is available from the Wiley Online Library or from the author.

Acknowledgements

The authors thank the U.K. EPSRC (grants EP/K007033/1, EP/K039547/1, EP/K016954/1, EP/M010619/1, and EP/G035954/1) and the North West Nanoscience Doctoral Training Centre (NOWNano DTC) for financial support. S.J.H. also thanks the Defence Threat Reduction Agency Grant HDTRA1-12-1-0013. N.S., J.R.B., and P.O.B. also thank the Parker family for funding their work. The authors also thank NEXUS at nanoLAB (Newcastle University) for XPS measurements. The authors also thank Robert Paulik for assistance in preparing the artwork. Data files can be obtained from http://www.mub.eps.manchester.ac.uk/robert-dryfe-electrochemistry/.

Received: January 26, 2016
Revised: April 4, 2016
Published online: July 27, 2016

[1] a) X. Huang, Z. Zeng, S. Bao, M. Wang, X. Qi, Z. Fan, H. Zhang, *Nat. Commun.* **2013**, *4*, 1444; b) T. F. Jaramillo, K. P. Jorgensen, J. Bonde, J. H. Nielsen, S. Horch, I. Chorkendorff, *Science* **2007**, *317*, 100.

[2] a) H. Wang, Z. Lu, S. Xu, D. Kong, J. J. Cha, G. Zheng, P.-C. Hsu, K. Yan, D. Bradshaw, F. B. Prinz, Y. Cui, *Proc. Natl. Acad. Sci. USA* **2013**, *110*, 19701; b) X. Zheng, J. Xu, K. Yan, H. Wang, Z. Wang, S. Yang, *Chem. Mater.* **2014**, *26*, 2344; c) H. Zhu, M. Du, M. Zhang, M. Zou, T. Yang, S. Wang, J. Yao, B. Guo, *Chem. Commun.* **2014**, *50*, 15435; d) M. Velický, M. A. Bissett, C. R. Woods, P. S. Toth, T. Georgiou, I. A. Kinloch, K. S. Novoselov, R. A. W. Dryfe, *Nano Lett.* **2016**, *16*, 2023.

[3] K. S. Novoselov, A. K. Geim, S. V. Morozov, D. Jiang, Y. Zhang, S. V. Dubonos, I. V. Grigorieva, A. A. Firsov, *Science* **2004**, *306*, 666.

[4] K. S. Novoselov, V. I. Falko, L. Colombo, P. R. Gellert, M. G. Schwab, K. Kim, *Nature* **2012**, *490*, 192.

[5] F. Bonaccorso, L. Colombo, G. Yu, M. Stoller, V. Tozzini, A. C. Ferrari, R. S. Ruoff, V. Pellegrini, *Science* **2015**, *347*, 1246501.

[6] a) A. K. Geim, I. V. Grigorieva, *Nature* **2013**, *499*, 419; b) C. Huang, S. Wu, A. M. Sanchez, J. J. P. Peters, R. Beanland, J. S. Ross, P. Rivera, W. Yao, D. H. Cobden, X. Xu, *Nat. Mater.* **2014**, *13*, 1096.

[7] a) Y. Li, H. Wang, L. Xie, Y. Liang, G. Hong, H. Dai, *J. Am. Chem. Soc.* **2011**, *133*, 7296; b) L. David, R. Bhandavat, G. Singh, *ACS Nano* **2014**, *8*, 1759.

[8] a) K.-J. Huang, L. Wang, Y.-J. Liu, Y.-M. Liu, H.-B. Wang, T. Gan, L.-L. Wang, *Int. J. Hydrogen Energy* **2013**, *38*, 14027; b) M. A. Bissett, I. A. Kinloch, R. A. W. Dryfe, *ACS Appl. Mater. Interfaces.* **2015**, *7*, 17388; c) J. Chen, C. Li, G. Shi, *J. Phys. Chem. Lett.* **2013**, *4*, 1244.

[9] a) M. Velicky, D. F. Bradley, A. J. Cooper, E. W. Hill, I. A. Kinloch, A. Mishchenko, K. S. Novoselov, H. V. Patten, P. S. Toth, A. T. Valota, S. D. Worrall, R. A. W. Dryfe, *ACS Nano* **2014**, *8*, 10089; b) A. G. Gueell, A. S. Cuharuc, Y.-R. Kim, G. Zhang, S.-y. Tan, N. Ebejer, P. R. Unwin, *ACS Nano.* **2015**, *9*, 3558; c) M. Velicky, M. A. Bissett, P. S. Toth, H. V. Patten, S. D. Worrall, A. N. J. Rodgers, E. W. Hill, I. A. Kinloch, K. S. Novoselov, T. Georgiou, L. Britnell, R. A. W. Dryfe, *Phys. Chem. Chem. Phys.* **2015**, *17*, 17844; d) D. A. C. Brownson, L. J. Munro, D. K. Kampouris, C. E. Banks, *RSC Adv.* **2011**, *1*, 978; e) A. Ambrosi, A. Bonanni, M. Pumera, *Nanoscale* **2011**, *3*, 2256; f) A. Ambrosi, M. Pumera, *J. Phys. Chem. C* **2013**, *117*, 2053.

© 2016 The Authors. Published by WILEY-VCH Verlag GmbH & Co. KGaA, Weinheim

[10] D. Kong, H. Wang, J. J. Cha, M. Pasta, K. J. Koski, J. Yao, Y. Cui, *Nano Lett.* **2013**, *13*, 1341.
[11] M. P. Cecchini, V. A. Turek, J. Paget, A. A. Kornyshev, J. B. Edel, *Nat. Mater.* **2013**, *12*, 165.
[12] Z. Samec, *Electrochim. Acta* **2012**, *84*, 21.
[13] a) S. Biswas, L. T. Drzal, *Nano Lett.* **2009**, *9*, 167; b) S. Gan, L. Zhong, T. Wu, D. Han, J. Zhang, J. Ulstrup, Q. Chi, L. Niu, *Adv. Mater.* **2012**, *24*, 3958.
[14] X. Yu, M. S. Prevot, N. Guijarro, K. Sivula, *Nat. Commun.* **2015**, *6*, 7596.
[15] a) V. H. Rodrigues de Souza, M. M. Oliveira, A. J. G. Zarbin, *J. Power Sources* **2014**, *260*, 34; b) P. S. Toth, A. N. J. Rodgers, A. K. Rabiu, R. A. W. Dryfe, *Electrochem. Commun.* **2015**, *50*, 6.
[16] P. S. Toth, M. Velicky, Q. M. Ramasse, D. M. Kepaptsoglou, R. A. W. Dryfe, *Adv. Funct. Mater.* **2015**, *25*, 2899.
[17] a) N. Zhu, S. Han, S. Gan, J. Ulstrup, Q. Chi, *Adv. Funct. Mater.* **2013**, *23*, 5297; b) N. Zhu, K. Zheng, K. J. Karki, M. Abdellah, Q. Zhu, S. Carlson, D. Haase, K. Žídek, J. Ulstrup, S. E. Canton, T. Pullerits, Q. Chi, *Sci. Rep.* **2015**, *5*, 9860; c) L. Zhang, J. Yu, M. Yang, Q. Xie, H. Peng, Z. Liu, *Nat. Commun.* **2013**, *4*, 1443.
[18] M. Al-Mamun, H. Zhang, P. Liu, Y. Wang, J. Cao, H. Zhao, *RSC Adv.* **2014**, *4*, 21277.
[19] A. Splendiani, L. Sun, Y. Zhang, T. Li, J. Kim, C.-Y. Chim, G. Galli, F. Wang, *Nano Lett.* **2010**, *10*, 1271.
[20] G. L. Frey, R. Tenne, M. J. Matthews, M. S. Dresselhaus, G. Dresselhaus, *Phys. Rev. B: Condens. Matter Mater. Phys.* **1999**, *60*, 2883.
[21] a) A. C. Ferrari, J. C. Meyer, V. Scardaci, C. Casiraghi, M. Lazzeri, F. Mauri, S. Piscanec, D. Jiang, K. S. Novoselov, S. Roth, A. K. Geim, *Phys. Rev. Lett.* **2006**, *97*, 187401; b) L. M. Malard, M. A. Pimenta, G. Dresselhaus, M. S. Dresselhaus, *Phys. Rep.* **2009**, *473*, 51.
[22] K.-G. Zhou, F. Withers, Y. Cao, S. Hu, G. Yu, C. Casiraghi, *ACS Nano* **2014**, *8*, 9914.
[23] H. Ago, H. Endo, P. Solis-Fernandez, R. Takizawa, Y. Ohta, Y. Fujita, K. Yamamoto, M. Tsuji, *ACS Appl. Mater. Interfaces* **2015**, *7*, 5265.
[24] S. M. Tan, A. Ambrosi, Z. Sofer, S. Huber, D. Sedmidubsky, M. Pumera, *Chem.–Eur. J.* **2015**, *21*, 7170.
[25] P. S. Toth, M. Velicky, Q. M. Ramasse, R. A. W. Dryfe, *Chem. Sci.* **2015**, *6*, 1316.
[26] a) Z. Saghi, X. Xu, Y. Peng, B. Inkson, G. Möbus, *Appl. Phys. Lett.* **2007**, *91*, 251906; b) P. A. Midgley, R. E. Dunin-Borkowski, *Nat. Mater.* **2009**, *8*, 271.
[27] M. Platt, R. A. W. Dryfe, E. P. L. Roberts, *Electrochim. Acta* **2004**, *49*, 3937.
[28] P. S. Toth, Q. M. Ramasse, M. Velicky, R. A. W. Dryfe, *Chem. Sci.* **2015**, *6*, 1316.
[29] P. S. Toth, A. T. Valota, M. Velicky, I. A. Kinloch, K. S. Novoselov, E. W. Hill, R. A. W. Dryfe, *Chem. Sci.* **2014**, *5*, 582.
[30] F. Li, L. Zhang, J. Li, X. Q. Lin, X. Z. Li, Y. Y. Fang, J. W. Huang, W. Z. Li, M. Tian, J. Jin, R. Li, *J. Power Sources* **2015**, *292*, 15.
[31] B. E. Conway, B. V. Tilak, *Electrochim. Acta* **2002**, *47*, 3571.
[32] D. Voiry, M. Salehi, R. Silva, T. Fujita, M. Chen, T. Asefa, V. B. Shenoy, G. Eda, M. Chhowalla, *Nano Lett.* **2013**, *13*, 6222.
[33] M. Beidaghi, C. Wang, *Adv. Funct. Mater.* **2012**, *22*, 4501.
[34] a) I. Hatay, P. Y. Ge, H. Vrubel, X. Hu, H. H. Girault, *Energy Environ. Sci.* **2011**, *4*, 4246; b) M. D. Scanlon, X. J. Bian, H. Vrubel, V. Amstutz, K. Schenk, X. L. Hu, B. H. Liu, H. H. Girault, *Phys. Chem. Chem. Phys.* **2013**, *15*, 2847; c) S. Rastgar, H. Deng, F. Cortes-Salazar, M. D. Scanlon, M. Pribil, V. Amstutz, A. A. Karyakin, S. Shahrokhian, H. H. Girault, *ChemElectroChem* **2014**, *1*, 59; d) E. Aslan, I. H. Patir, M. Ersoz, *ChemCatChem* **2014**, *6*, 2832; e) E. Aslan, I. Akin, I. H. Patir, *ChemCatChem* **2016**, *8*, 719.
[35] S. Hu, M. Lozada-Hidalgo, F. C. Wang, A. Mishchenko, F. Schedin, R. R. Nair, E. W. Hill, D. W. Boukhvalov, M. I. Katsnelson, R. A. Dryfe, I. V. Grigorieva, H. A. Wu, A. K. Geim, *Nature* **2014**, *516*, 227.
[36] J. J. Nieminen, I. Hatay, P. Ge, M. A. Mendez, L. Murtomaki, H. H. Girault, *Chem. Commun.* **2011**, *47*, 5548.
[37] E. Aslan, I. H. Patir, M. Ersoz, *Chem.–Eur. J.* **2015**, *21*, 4585.
[38] I. Hatay, B. Siu, F. Li, R. Partovi-Nia, H. Vrubel, X. Hu, M. Ersoz, H. H. Girault, *Angew. Chem., Int. Ed.* **2009**, *48*, 5139.
[39] a) J. N. Coleman, M. Lotya, A. O'Neill, S. D. Bergin, P. J. King, U. Khan, K. Young, A. Gaucher, S. De, R. J. Smith, I. V. Shvets, S. K. Arora, G. Stanton, H.-Y. Kim, K. Lee, G. T. Kim, G. S. Duesberg, T. Hallam, J. J. Boland, J. J. Wang, J. F. Donegan, J. C. Grunlan, G. Moriarty, A. Shmeliov, R. J. Nicholls, J. M. Perkins, E. M. Grieveson, K. Theuwissen, D. W. McComb, P. D. Nellist, V. Nicolosi, *Science* **2011**, *331*, 568; b) C. M. Orofeo, S. Suzuki, Y. Sekine, H. Hibino, *Appl. Phys. Lett.* **2014**, *105*, 083112.

© 2016 The Authors. Published by WILEY-VCH Verlag GmbH & Co. KGaA, Weinheim